

Near-Field Phase-Contrast Imaging of Micropores in Silicon Carbide Crystals with Synchrotron Radiation

Victor G. Kohn and Tatiana S. Argunova*

The results of in-line phase-contrast imaging of micropores in crystals with synchrotron radiation (SR) using an example of silicon carbide (SiC) single crystal are reported. Computer simulations of micropore images have provided a thorough interpretation of specific features of experimental results. Herein, micropores of sizes in the interval from a few micrometers to several tens of micrometers are analyzed. The near-field condition is realized only on a short distance behind the sample for such dimensions. In addition, the size of experimental images is below the resolution limit of the best possible charge-coupled device detectors. Therefore, it is impossible to determine the actual transverse dimensions directly under the near-field experiment. A new experimental setup is proposed that employs a secondary SR source created by a compound refractive lens at the focus. Two conditions have to be satisfied. First, the focus must be located in front of the sample at a short distance. Second, the beam size at the focus has to be as small as possible. The implementation of the new scheme requires a high-intensity synchrotron or X-ray laser beam provided by modern X-ray radiation sources. Computer simulations of a virtual experiment using this new method are performed.

Large-area SiC is used as a closely lattice-matched foreign substrate for the growth of aluminum nitride (AlN) crystal as recently reviewed by Sumathi.^[8] AlN is another example of a single crystal with voids and microcracks.^[9,10] Structural inhomogeneities negatively affect the performance of devices fabricated on SiC or AlN crystalline substrates. Thermal destruction of the SiC surface is a promising technology for producing graphene films.^[11] However, the relationship between substrate uniformity and the quality of graphene films is not well understood. Therefore, diagnostic methods and quantitative research techniques for determining the size and density of micropores in single crystals have been under active development.

The in-line X-ray phase-contrast imaging variation of electron density is widely used after 1995, when Snigirev et al.^[12] have shown that the synchrotron radiation (SR) sources of the third generation can provide

a sufficient degree of coherence. This technique is relatively simple. Nevertheless, it allows immediate and fast visualization of any electron density variation inside the material. It is also applicable to micropores in single crystals. Unfortunately, images of micropores can be registered only at a long sample-to-detector distance (far-field region) when the image size enlarges to the extent that a high-resolution charge-coupled device (CCD) can detect.

However, the actual pore size can be obtained only after an inverse problem solution in the far-field region of imaging. The goal is the phase of the transmission function of the object, which is proportional to the total electron density along the beam path. It can be determined, for example, using computer simulations. Many studies utilized polychromatic radiation (see, e.g., Ref. [13]) or a pink SR beam.^[14,15] The intensity of the monochromatic beam was not sufficient to allow fast detection of weak contrast.

This article presents the result of a phase-contrast imaging experiment with monochromatic radiation. After a survey inspection of SiC and AlN samples, we chose the image containing two kinds of pores in the same place: tiny pores of μm -scale transverse size and large pores with a transverse dimension of several tens of microns. The image allowed us to analyze the large pore for the first time. Furthermore, we performed computer simulations and theoretical analyses to interpret all features of this image.


We know that a phase-contrast image shows the actual transverse size of the object if this size is much larger than the diameter of the first Fresnel zone. However, this occurs at a very short

1. Introduction

Imperfect single crystals contain defects such as cracks, pipes, and pores, limiting their range of applications. Pipes with μm -sized diameters were observed in silicon carbide (SiC) crystals, ferrite garnets, Y–Ba–Cu oxide, quartz, and gallium nitride. A striking example of primary pore formation is the crystallization of SiC, which is a promising material for wide bandgap semiconductor devices.^[1] The micropores were often associated with subgrain boundaries,^[2] a polytype instability,^[3,4] and a seed fixation.^[5,6] A micropipe (MP) is the most harmful defect consisting of a hole around a core of super-dislocation. Although MPs were eliminated from commercial SiC substrates,^[7] the production of wafers with a low density of pores is still costly.

V. G. Kohn
National Research Centre “Kurchatov Institute”
123182 Moscow, Russia

T. S. Argunova
Division of Physics of Dielectric and Semiconductors
Ioffe Institute RAS
Polytekhnikeskaya st. 26, 194021 St. Petersburg, Russia
E-mail: argunova@mail.ioffe.ru

 The ORCID identification number(s) for the author(s) of this article can be found under <https://doi.org/10.1002/pssb.202100651>.

DOI: 10.1002/pssb.202100651

distance between the sample and the detector for tiny pores. In addition, the spatial resolution of the best detectors is not good enough to obtain a high-quality image of such small objects. Therefore, in this article, we propose and analyze a new experimental setup. It contains a secondary source of SR as the focus of a compound refractive lens (CRL), used for the first time by Snigirev et al.^[16]

CRL is located at a short distance in front of the sample. This scheme allows one to record magnified images in almost the near-field region. The degree of magnification is proportional to the sample-to-detector distance. In this setup, the transverse beam size at the focus has to be as small as possible. Specifically, it has to be much smaller than the transverse size of the object. Therefore, the implementation of the new scheme requires high-intensity synchrotron or X-ray laser beam provided by modern X-ray radiation sources. Computer simulations of a virtual experiment in the new scheme have been performed.

The following section presents the experimental result. The third section contains fundamentals of theory, data processing, and computer simulations. Finally, in the fourth section, we describe a new experimental scheme with a secondary source and perform computer simulations of the images of a model object.

2. Experimental Result

Experimental studies of micropores were carried out at Pohang Light Source in Pohang, South Korea. It is a third-generation medium-brilliant SR source operating with total electron energy of 3 GeV. At the imaging beamline, a multilayer mirror provided the monochromatic beam. In this case, the beam's spectral width was broader than that of crystal monochromators. Therefore, more photons were available for measurements of weak phase-contrast images. In contrast, phase-contrast images are less sensitive to the wavelength variation than Bragg diffraction images, and a high degree of monochromatization is not required.

The experimental scheme was described in our previous articles (e.g.,^[17]). The main advantage of the setup was the detector with a high resolution provided by projecting a luminescence image (magnified via an optical objective) onto the CCD detector. We used 20× magnification, which reduced the effective pixel size to 0.275 μm. **Figure 1** shows a part of the image recorded by the detector positioned at a distance of $z_1 = 40$ cm from the sample.

The feature of this fragment is the presence of pores with different sizes located near each other. The leftmost pore is large. Three smaller pores are visible at the right. The tiny pores have different transverse sizes, but their images do not differ significantly from each other. The size manifests itself through a brighter contrast of the central area, as shown by Kohn et al.^[17]

The image structure depends on the ratio S_0/D_1 , where S_0 is the transverse size of a micropore, $D_1 = 2(\lambda z)^{1/2}$ is the diameter of the first Fresnel zone. Here, $\lambda = hc/E$ is the radiation wavelength, h is the Planck constant, c is the speed of light, and E is the photon energy. For the image in **Figure 1**, $D_1 = 11$ μm. Therefore, $S_0 > D_1$ for the large pore, that is just the near-field condition when the image shows only the object's boundaries.

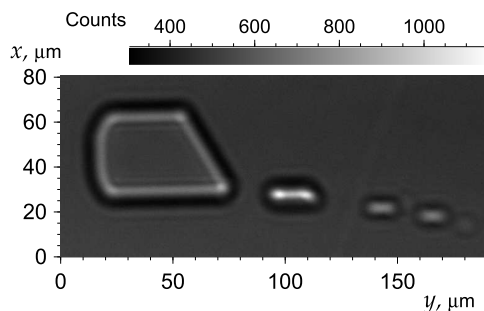


Figure 1. Experimental phase-contrast image of a crystal region containing pores of different sizes. 6H-SiC sample thickness 50 μm. $E = 16$ keV, $z_1 = 40$ cm. Multilayer monochromator $\Delta E/E = 0.4\%$.

However, the images are more complex for the small pores, where $S_0 < D_1$. The extreme case of microscopic pores was considered by Kohn et al.^[17] analytically.

We present the experimental results obtained using a beam that emerges at the bending magnet source with the size 160 (H) × 60 (V) μm² at the distance of $z_0 = 34$ m from the sample. The projections of the source dimensions at the detector plane, calculated by multiplying the actual source sizes by the distance ratio z_1/z_0 , equal to $V_d = 0.7$ μm and $H_d = 1.9$ μm. Horizontal smoothing must impact the image more significantly than vertical smoothing. However, in **Figure 1**, no difference is observed. This effect is explained in the next section. We note that the x and y axes of **Figure 1** direct vertically and horizontally.

3. Theory

The method of in-line phase-contrast imaging of micro-objects with SR of the third generation was used for the first time by Snigirev et al.^[12] In that work, the first variant of the theory was also presented. It is relatively simple. Later, many papers and review articles described the phase-contrast theory, for example.^[15,18] Finally, researchers used the approach for computer simulations with the aim of imaging system optimization^[19] and investigating micropores.^[20,21] Here, we present several equations, which have been used in our computer simulations. For the sake of simplicity, the equations for 2D objects (homogeneous along the y direction) are considered in the plane (x, z). Generalization to the 3D objects is similar and easy to perform, but equations are more complex. As is known, SR is emitted by electrons moving on a circular orbit in a ring with a speed close to the speed of light. The relativistic electrons emit spontaneously in pulses much shorter in width than the measurement time. Therefore, to simulate the experimental data accurately, we have to use a model where only monochromatic harmonics of radiation from individual points of the source are coherent.

It means that one should decompose the radiation spectrum into monochromatic harmonics, solve Maxwell equations for the wave generated at the point x_s on the source plane axis x , and then sum over intensities of waves at the detector from different harmonics and different source points. To do so, we will assume that a large divergent beam illuminates the entire object, and we are not interested in the actual size of the beam. Then, the wave

function of X-ray radiation can be decomposed into a product of fast and slow functions.

$$E(x, x_s, t) = \exp(ikz - i\omega t)A(x, x_s, \omega), \quad (1)$$

$$A(x, x_s) = \int dx_o P(x - x_o, z_1) T(x_o) P(x_o - x_s, z_0) \quad (2)$$

Here

$$T(x) = \exp(ik(\delta - i\beta)t(x)) \quad (3)$$

is the transmission function of a micropore within the material. Optical constants δ and β characterize a complex refractive index of the material $n = 1 - \delta + i\beta$, and $t(x)$ is the path length of the ray at the x point inside the pore. We assume that approximately all rays parallel the optical axis (the z axis) inside the pore.

$$P(x, z) = (i\lambda z)^{-1/2} \exp(ixx^2/\lambda z) \quad (4)$$

is the Fresnel propagator, which represents the transverse part of a spherical monochromatic wave in the paraxial approximation.

The structure of Equation (2) has a clear physical meaning. X-ray radiation from a point source at a distance z_0 from the sample illuminates the sample; the latter contributes a factor $T(x)$ to the wave function. According to the Huygens–Fresnel principle, further propagation of radiation on the distance z_1 is described by a convolution of the wave function and the Fresnel propagator. However, the equation itself does not provide any information about the image properties. Mathematics allows us to obtain this information in the general case. Using Equation (4), we rewrite Equation (2) in another form, namely

$$A(x, x_s) = P(x - x_s, z_t) a(X, Z), \quad (5)$$

$$a(X, Z) = \int dx_o P(X - x_o, Z) T(x_o), \quad (6)$$

$$z_t = z_0 + z_1, \quad Z = z_0 z_1 / z_t, \quad X = \frac{z_0}{z_t} \left(x + x_s \frac{z_1}{z_0} \right) \quad (7)$$

We note that the first factor in Equation (5) does not influence the intensity, and only the function $a(X, Z)$ describes the image.

For numerical calculations, this function can be transformed into the expression

$$a(X, Z) = 1 + \int dx_o P(X - x_o, Z) [T(x_o) - 1] \quad (8)$$

that follows from the normalization of the Fresnel propagator. Equation (8) has an integral with finite limits advantage because the integrand equals zero outside the micropore, where $T(x) = 1$. This fact is essential for computer simulations based on fast Fourier transform method.

We performed computer simulations employing a multipurpose program called X-Ray Wave Propagation, 1D (XRWP1), which can simulate SR beam propagation in the experimental setup of an imaging beamline at SR source. The program is under permanent development using the programming language ACL.^[22] Features of phase-contrast imaging of small pores have already been analyzed.^[15,20,21] However, large pores have attracted less attention than micropores. That is why we study

the large pore in Figure 1 in this work. The vertical sections represent the most exciting part of the image due to the small source size in the vertical direction.

We note that the experimental image shown in Figure 1 was obtained as 17 exposures taken sequentially over a short time interval. All 17 snapshots look the same because of a relatively low resolution. However, the images were captured in tiff format within a counting range from 0 to 65 535. In a real-life experiment, the maximum number of photons is slightly more than 1000. Nevertheless, a more accurate presentation shows noise-induced oscillations anyway. Moreover, the intensity curves for different images become different in the same range as the noise oscillations.

Figure 2 shows the vertical section of Figure 1 for $y = 43.7 \mu\text{m}$. This figure simultaneously displays all the 17 curves drawn with thin black lines. The total line width shows the noise level on each curve, and the shading density indicates that the different lines do not coincide, although they have approximately the same amount of noise. A yellow curve was obtained by summing all the 17 curves and dividing them by 17. One can see that the yellow curve has a significantly lower noise level compared to the black one. Moreover, additional oscillations with a smaller amplitude are observed at the main minimum and maximum tails. They are visible even in Figure 1, and all the 17 copies of the series display them.

Our experience in the phase-contrast simulations allowed us to conclude that the image profile with the dispersion peculiarities at the edges corresponds to a flat pore with rounded edges. Therefore, we chose a pore model having a vertical section like a rectangle with edges of the shape of semicircles. The diameter of semicircles is equal to the rectangle's width, which equals the thickness of a flat part of the pore along the beam path. This section is shown in Figure 3. Two parameters describe the object: the length $w = h + d$ along the axis x and the thickness d along the axis z . Here, h is the length of the flat part (the height of the rectangle).

The length w is usually slightly less than the distance between the minima of the image profile. The minimums are formed due to a deflection of rays to the center of the pore due to refraction. As a result, the intensity is minimal at the object's edges. The object's thickness d influences the image contrast. We determined it by simulations. The result of the simulations is shown in Figure 4. The experimental parameters were mentioned earlier and $w = 44 \mu\text{m}$, $d = 6 \mu\text{m}$.

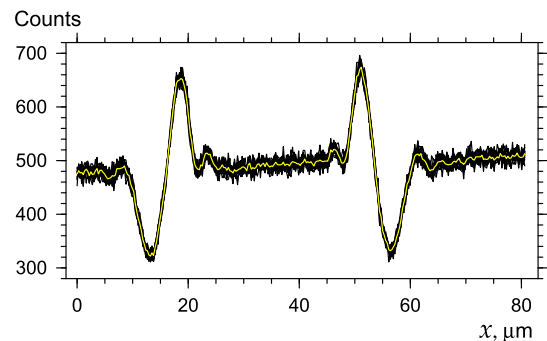


Figure 2. The vertical section of the image in Figure 1; $y = 43.7 \mu\text{m}$.

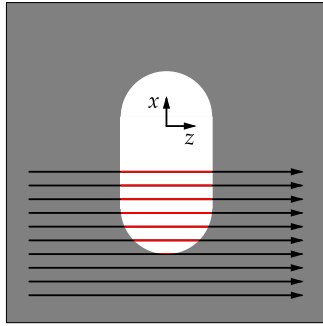


Figure 3. A model simulating a pore. Red parts of rays define $t(x)$.

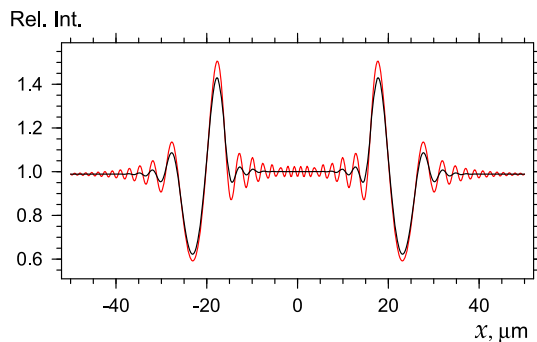


Figure 4. Curves represent the relative intensity calculated for a model object.

The red curve corresponds to the convolution of the curve calculated for a point source with a Gaussian function, which has full width at half maximum $V_d = 0.7 \mu\text{m}$. This value corresponds to the projection of the vertical source size to the detector plane. However, the red curve does not match the experimental profile. The black curve is calculated for $V_d = 2 \mu\text{m}$, close to H_d . This curve simulates the experimental one much better. Thus, our calculation has shown that smoothing the experimental curve occurs due to not just the source size. One can consider several other smoothing origins. For example, we want to specify the insufficient stability of the mechanical system implemented and the electron bunch position inside the ring. Computer simulation allows us to gain additional information about the experiment, even if the object's transverse size is directly available from the experimental image.

4. Secondary Source Experimental Setup

It follows from Equation (7) that the properties of the image depend on the effective distance $Z = z_0 z_1 / z_i$. The following relation is fulfilled in a standard SR phase-contrast imaging setup: $z_0 \gg z_1$. Therefore, Z is very close to z_1 (only a little less). In addition, very little difference between the image size and the object size occurs because X is close to x . Figure 5a shows this variant of the setup. In such a scheme, the projection of the source size is much smaller than the source size itself, which allows the use of the source with relatively large size. A small value of Z is achieved using a small value of z_1 .

However, there is another possibility to obtain a small value of Z and implement the near-field regime. We can realize the inverse relationship $z_0 \ll z_1$. This case is shown in Figure 5b. In such a case, the experimental image corresponds to the near-field condition, but the image size will be much larger than the object size. We note that recording a high-quality image with a medium-resolution CCD is highly desirable.

At the same time, the projection of the source size also increases, as shown in the figure. The high resolution can be attained only when the transverse source size is smaller than the object size. Available microfocus laboratory sources have an X-ray spot size of more than $1 \mu\text{m}$. Such a scheme can be effective when studying objects with a size of more than $10 \mu\text{m}$.

A secondary source is required to implement such a scheme with SR source, which, for example, can be created utilizing a CRL, first proposed by Snigirev et al.^[16] Today, the planar parabolic CRL can create a beam of size less than 100 nm .^[23] However, the theoretical limit is much less. Figure 5c presents an outline of the setup based on such a scheme. Analytical theory of imaging and focusing by CRL was first developed by Kohn^[24,25] and later by Kohn and Folomeshkin.^[26] The latter work showed that the theoretical limit for the beam size at the focus is equal to $w_c = \lambda / (8\delta)^{1/2}$. It is reached at sufficiently high energies and a small aperture of CRL when the role of absorption becomes not essential.

For example, the limit value for the planar parabolic CRL made of silicon^[23] equals 20 nm . When conditions are changed, the beam will have a larger size; but the value of 100 nm is accessible quite easily. Planar parabolic CRLs make the beam focus only in one direction, and they have a short focal length. Long focal length CRL of large aperture, including those for focusing in two directions, has the beam size at focus in the submicron range.

Thus, images of microscopic pores cannot be resolved with reasonable accuracy in two directions simultaneously. However, planar CRLs can be used for focusing in two mutually orthogonal directions consistently. Another restriction of this technique in the near-field region is that the beam behind the focus has a relatively small angular divergence. For this reason, one is unable to bring the sample directly in front of the focus

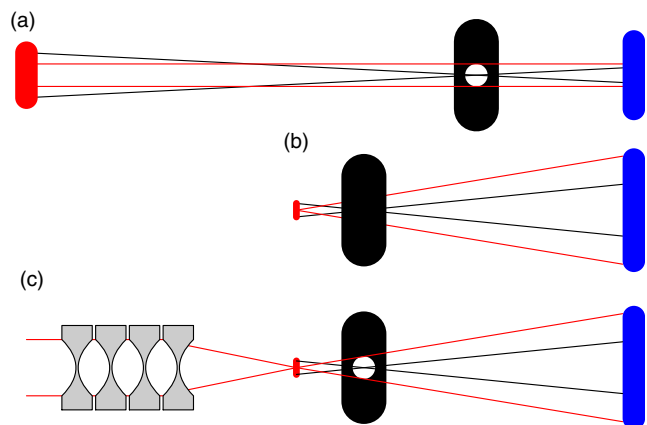


Figure 5. Experimental schemes considered in this article. See text for details.

because the wavefront will not be sufficient to illuminate the sample entirely.

We performed the computer simulations employing the XRWP1 program under the following experimental conditions: photon energy $E = 12$ keV, the distance between the point SR source and CRL $z_s = 50$ m, the parameters of the planar parabolic CRL (made of silicon) correspond to those used in work by Snigirev et al.^[27] Namely, the aperture $A = 50$ μm , the length of one biconcave element $p_1 = 102$ μm , the radius of elemental lens surface curvature $R = 6.25$ μm , and the thickness of the thin part between two surfaces $d_1 = 2$ μm . Such a lens composed of $n_1 = 100$ elements focuses a parallel beam at the distance $f = 0.556$ cm from the endpoint of the CRL, and its length is $L = 1.02$ cm. The beam size at the focus, calculated with the online program,^[28] was 68 nm. It is a theoretical estimate. Experiments are still unable to obtain the same size of the beam.

A slit in front of the lens has the same size as an aperture. However, its effect is practically negligible: the X-ray beam at the exit of the CRL is compressed down to a size of 3.7 μm . Therefore, the beam is mainly focused inside the CRL. We chose a cylindrical MP as a model object. MP within a SiC crystal had a diameter of 2 μm . The crystal was placed at a distance of 2.556 cm from the endpoint of CRL. As a result, we obtained the distance 2 cm from the object (MP) to the secondary source, that is, the beam at the focus spot. **Figure 6** contains the images of the MP calculated at a distance of 5 cm (red line) and 10 cm (black line) from the MP. The size of the secondary source is taken into account for the calculated intensity profiles shown in the figure.

The curves of **Figure 6** present the intensity ratio at the detector to the intensity in front of the CRL. One can see that the CRL reduces the peak intensity by 10 times at a distance of 5 cm. Further, the intensity decreases with the distance according to the linear law. This law is easy to understand because the image size increases with the distance, but the integrated intensity remains unchanged. The figure clearly shows that the MP image, recorded at a distance of 5 cm, is at the top of the Gaussian curve, which represents a full width of the beam focused by the CRL.

We should note that the image size increases simultaneously with the beam width, and the black curve within a broader range has the same outline as the red curve. The properties of the image recorded using such a scheme are practically independent of the distance z_1 behind the object, and it is wholly determined by the distance z_0 between the secondary source and the object. In

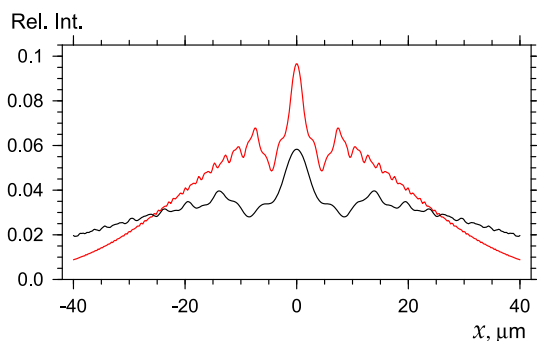


Figure 6. Simulated images of the MP cross section at a distance of 5 cm (red) and 10 cm (black) from the object.

contrast, this image is entirely consistent with that recorded using the standard set up at a distance $z_1 = 2$ cm behind the object.

We further note that the calculations show a very weak dependence of the image on the actual source size. It means that one can achieve stronger coherence by focusing the beam by the CRL. Consequently, one can implement the setup described above in second-generation synchrotron light sources with a relatively large angular size.

Acknowledgements

SR experiments performed by T.S.A. were supported by the Ministry of Science and Higher Education of the Russian Federation (agreement no. 075-15-2021-1349). Computer simulations were done by V.G.K. with the support of the Russian Foundation for Basic Research (RFBR) (grant no. 19-29-12043mk) and the Ministry of Science and Higher Education of the Russian Federation (agreement no. 075-15-2021-1362).

Conflict of Interest

The authors declare no conflict of interest.

Data Availability Statement

The data that support the findings of this study are available from the corresponding author upon reasonable request.

Keywords

micropores in single crystals, phase contrast, synchrotron radiation, X-ray imaging

Received: December 16, 2021

Revised: January 25, 2022

Published online: February 19, 2022

- [1] A. A. Lebedev, P. A. Ivanov, M. E. Levinshtein, E. N. Mokhov, S. S. Nagalyuk, A. N. Anisimov, P. G. Baranov, *Phys.-Usp.* **2019**, *62*, 754.
- [2] T. S. Argunova, M. Yu. Gutkin, J. H. Je, J. H. Lim, E. N. Mokhov, A. D. Roenkov, *CrystEngComm.* **2014**, *16*, 8917.
- [3] D. Siche, H. J. Rost, J. Doerschel, D. Schulz, J. Wollweber, *J. Cryst. Growth* **2002**, *237–239*, 1187.
- [4] M. Yu. Gutkin, A. G. Sheinerman, T. S. Argunova, J. M. Yi, M. U. Kim, J. H. Je, S. S. Nagalyuk, E. N. Mokhov, G. Margaritondo, Y. Hwu, *J. Appl. Phys.* **2006**, *100*, 093518.
- [5] Z. G. Herro, B. M. Epelbaum, M. Bickermann, C. Seitz, A. Magerl, A. Winnacker, *J. Cryst. Growth* **2005**, *275*, 496.
- [6] J. L. Liu, J. Q. Gao, J. K. Cheng, J. F. Yang, G. J. Qiao, *J. Mater. Sci.* **2007**, *42*, 6148.
- [7] T. Kimoto, *Prog. Cryst. Growth Charact. Mater.* **2016**, *62*, 329.
- [8] R. R. Sumathi, *ECS J. Solid State Sci. Technol.* **2021**, *10*, 035001.
- [9] R. R. Sumathi, P. Gille, *J. Mater. Sci.: Mater. Electron.* **2014**, *25*, 3733.
- [10] T. S. Argunova, M. Yu. Gutkin, K. D. Shcherbachev, J. H. Je, J. H. Lim, O. P. Kazarova, E. N. Mokhov, *J. Mater. Sci.* **2017**, *52*, 4244.

- [11] A. A. Lebedev, S. Yu. Davydov, I. A. Eliseyev, A. D. Roenkov, O. Avdeev, S. P. Lebedev, Yu. Makarov, M. Puzyk, S. Klotchenko, A. S. Usikov, *Materials* **2021**, *14*, 590.
- [12] A. Snigirev, I. Snigireva, V. Kohn, S. Kuznetsov, I. Schelokov, *Rev. Sci. Instrum.* **1995**, *66*, 5486.
- [13] T. E. Gureyev, S. W. Wilkins, *Opt. Commun.* **1998**, *147*, 229.
- [14] S. C. Mayo, W. Andrew, A. W. Stevenson, S. W. Wilkins, *Materials* **2012**, *5*, 937.
- [15] T. S. Argunova, V. G. Kohn, *Phys.-Usp.* **2019**, *62*, 602.
- [16] A. Snigirev, V. Kohn, I. Snigireva, B. Lengeler, *Nature* **1996**, *384*, 49.
- [17] V. G. Kohn, T. S. Argunova, J. H. Je, *J. Phys. D: Appl. Phys.* **2010**, *43*, 442002.
- [18] M. Endrizzi, *Nucl. Instrum. Methods Phys. Res., Sect. A* **2018**, *878*, 88.
- [19] Ya. I. Nesterets, S. W. Wilkins, T. E. Gureyev, A. Pogany, A. W. Stevenson, *Sci. Instrum.* **2005**, *76*, 093706.
- [20] S. Agliozzo, P. Cloetens, *J. Microscopy* **2004**, *216*, 62.
- [21] S. Zabler, H. Riesemeier, P. Fratzl, P. Zaslansky, *Opt. Express* **2006**, *14*, 8584.
- [22] V. G. Kohn, *ACL Programming Language*, **2006**, <http://kohnvict.ucoz.ru/acl/acl.htm> (accessed: January 2022).
- [23] A. Snigirev, I. Snigireva, M. Grigoriev, V. Yunkin, M. Di Michiel, G. Vaughan, V. Kohn, S. Kuznetsov, *J. Phys. Conf. Ser.* **2009**, *186*, 012072.
- [24] V. G. Kohn, *JETP Lett.* **2002**, *76*, 600.
- [25] V. G. Kohn, *JETP* **2003**, *97*, 204.
- [26] V. G. Kohn, M. S. Folomeshkin, *J. Synchrotron Radiat.* **2021**, *28*, 419.
- [27] A. Snigirev, I. Snigireva, V. Kohn, V. Yunkin, S. Kuznetsov, M. B. Grigoriev, T. Roth, G. Vaughan, C. Detlefs, *Phys. Rev. Lett.* **2009**, *103*, 064801.
- [28] V. G. Kohn, *X-ray CRL Parameters*, **2018**, <http://kohnvict.ucoz.ru/jsp/1-crlpar.htm> (accessed: January 2022).